COMMUNICATION

Check for updates

Enhancing the selectivity of C_2 hydrocarbons over Fe-based catalysts by controlling nitrogen doping in electrocatalytic CO_2 reduction†

Peng Chen,[a,b] Shiqiang Liu,[a] Pei Zhang,*[a] Xinchen Kang, [ID] [a,b] Xing Tong,[a,b] Jun Ma, [ID] [a] Chunjun Chen,[a] Zhimin Liu, [ID] [a,b] Xueqing Xing,[c] Zhonghua Wu, [ID] [c] Lirong Zheng [ID] [c] and Buxing Han [ID] *[a,b,d]

Rational design of cost-effective materials as highly efficient catalysts for the electrochemical CO_2 reduction reaction (CO_2RR) to produce multi-carbon (C_{2+}) hydrocarbons is highly desirable. Cu-based catalysts are widely recognized as effective for the electrosynthesis of multi-carbon products. Exploration of non-copper-based catalysts for C_{2+} products is very interesting and challenging. In this work, using ethylenediaminetetraacetic acid disodium salt and ethylenediamine as the ligands and N source, N-doped Fe_2O_3 catalysts containing $FeO_{1-x}N_x$ ($0.34 < x < 0.54$) sites with and without a FeN_4 structure were fabricated. It was found that the catalyst without a FeN_4 structure converted CO_2 to C_2 hydrocarbons (ethane and ethylene). The faradaic efficiency (FE) of C_2 products and the current density of C_2 products reached 60.8% and 39.1 mA cm^{-2}, respectively, which is currently the best result for non-copper catalysts in an H-cell. However, the FE of the catalyst with a FeN_4 structure was much lower when producing C_2 products. Detailed study showed that the $FeO_{1-x}N_x$ sites with suitable coordination of N with Fe was pivotal to the high FE of C_2 products. A combination of experimental and density functional theory studies indicated that the feasible coordination of N with Fe resulted in the deformation of the electron cloud around the Fe nucleus, which facilitated the charge transfer and promoted the production of C_2 products. This work provides a successful example of designing non-copper catalysts for producing C_{2+} products in the CO_2RR.

Green foundation

1. We report N-doped Fe_2O_3 catalysts containing $FeO_{1-x}N_x$ ($0.34 < x < 0.54$) sites with and without a FeN_4 structure. It was found that the performance for the catalyst without a FeN_4 structure was excellent for the electroanalytic CO_2 reduction reaction to produce C_2 hydrocarbons (ethane and ethene).

2. The faradaic efficiency (FE) and current density of C_2 products reached 60.8% and 39.1 mA cm^{-2}, respectively, which is currently the best result for non-copper catalysts in an H-cell. This work provides a successful example of designing non-copper catalysts for producing C_{2+} products from the CO_2RR.

3. In future studies, the utilization of flue gas as a direct raw material for carbon dioxide sources will be explored, considering the excellent ability of ionic liquid to capture CO_2. This type of approach could be more cost-effective in practical application. Moreover, realizing high efficiency for the formation of C_{2+} products in inexpensive, and more easily recyclable electrolytes over Fe-based catalysts is an interesting topic for future research. Furthermore, other efficient non-copper catalysts, such as multi-metal catalysts, should be designed for producing C_{2+} products, and the relationship between composition, structure, and efficiency should be disclosed.

[a]*Beijing National Laboratory for Molecular Sciences, CAS Key Laboratory of Colloid and Interface and Thermodynamics, CAS Research/Education Center for Excellence in Molecular Sciences, Center for Carbon Neutral Chemistry, Institute of Chemistry, Chinese Academy of Sciences, Beijing 100190, China. E-mail: zhangpei@iccas.ac.cn, hanbx@iccas.ac.cn*

[b]*School of Chemistry, University of Chinese Academy of Sciences, Beijing 100049, China*

[c]*Beijing Synchrotron Radiation Facility, Institute of High Energy Physics, Chinese Academy of Sciences, Beijing 100049, China*

[d]*Shanghai Key Laboratory of Green Chemistry and Chemical Processes, School of Chemistry and Molecular Engineering, East China Normal University, Shanghai 200062, China*

†Electronic supplementary information (ESI) available. See DOI: https://doi.org/10.1039/d5gc00678c

Introduction

The conversion of carbon dioxide (CO_2) to high value-added chemicals or fuels under ambient temperature is considered as a promising and effective approach to solve the greenhouse effect problem.[1,2] Many efforts have been devoted to achieving carbonaceous products by constructing various electrocatalysts, such as Cu-, Fe-, Co-, Ni-, and Zn-based materials, for the electrochemical CO_2 reduction reaction (CO_2RR).[3–7] The use of earth-abundant catalysts for the electrocatalytic reduction of CO_2 to carbonaceous products is desirable. Iron is the most inexpensive and one of the most abundant transition metals, and iron-based catalysts have been extensively studied for

CO_2RR, which mainly produces C_1 products such as CO with high efficiency and selectivity.[8–11] The further conversion of CO_2 into more energy-intensive, higher-value C_2 products is desirable, but still remains a challenge.

In recent years, the activity for generating C_2 products has been enhanced by introducing elemental dopants such as S, P, and N into Fe-based catalysts, which indeed promotes the production of C_2 products.[12] However, the efficiency of the CO_2RR in obtaining C_{2+} products is far from satisfactory. Additionally, the nature of the active sites responsible for C–C coupling in Fe-based catalysts continues to remain elusive to date.

Additional studies have verified that metal centers are crucial for the CO_2RR. It was reported that dispersed M–N_x (M = Mn, Fe, Ni) sites in electrocatalysts exhibited high faradaic efficiency (FE) for CO.[13] It can be concluded that metal sites rich in elemental N are feasible for producing C_1 products, which was attributed to the desorption of *CO intermediates over M–N_x sites.[14–18] In a previous work,[19] we also found that the variation of N coordination with Fe in iron-based catalysts resulted in different selectivity toward C_1 or C_2 products in the CO_2RR.

Based on experimental results and previous reports, it is speculated that the desorption of *CO prevents further transformations for C–C coupling to generate C_{2+} products.[20–23] Therefore, it is expected that developing catalysts to tune the adsorption ability of *CO will realize the reaction routes toward C–C coupling during the CO_2RR. In other words, the Fe–N_x sites that are in favor of desorbing *CO intermediates should be avoided in the catalysts. However, iron-based catalysts with N dopant can generally be obtained in one pot by annealing iron hydroxides at elevated temperatures in the presence of a N source. It is inevitable that certain single- or double-active centers will be generated. Moreover, Fe–N_x sites will usually form due to the feasible migration of N during the preparation. Precise regulation of N–Fe–O sites in the doping process to further tune the selectivity towards C_{2+} products is a promising method.

Herein, we designed an approach to control the appropriate Fe–N/O coordination by utilizing the competitive coordination of Fe^{2+} and Cu^{2+} precursors with ethylenediaminetetraacetic acid disodium salt (EDTA-2Na, YH_2) and ethylenediamine (EDA) at different pH values. To distinguish the different structures of EDTA at different pH values, Y was used to represent EDTA with four COO^- units and YH_2 to represent EDTA with two COO^- units. The obtained precipitates were pyrolyzed under an N_2 atmosphere, and catalysts containing different N occupancies in N–Fe–O sites were acquired. It was demonstrated that the catalyst possessing N–Fe–O sites without a FeN_4 structure was very efficient for the CO_2RR to produce C_2 hydrocarbons, including ethane and ethylene. The faradaic efficiency (FE) of C_2 products and the current density of C_2 products reached 60.8% and 39.1 mA cm^{-2}, respectively, which is the best result for non-copper catalysts in an H-cell to date. However, the catalyst containing a FeN_4 structure showed much lower FE for C_2 products. The correlation of catalytic performances and various N–Fe–O sites with different N occu-

pancies was explored by a combination of experimental results and density functional theory (DFT) study.

Results and discussion

The coordination between metal ions and chelators (YH_2 and EDA) is a dynamic process. YH_2 exhibits various conformations with different association constants under varied pH conditions, resulting in different abilities to chelate with metal ions.[24–26] Based on this principle, we propose a strategy to use competitive coordination to fabricate N-doped iron oxide.

YH_2 was dissolved in deionized water, and after the preferential addition of an excess amount of $FeSO_4$ into the YH_2 solution to ensure the saturated coordination of YH_2 with Fe^{2+}, $CuSO_4$ and EDA were successively added to the solution. During the process, the reaction flask was sealed. The exact molar ratios are shown in Table S1.† As illustrated in Fig. 1a: stage I: the equilibrated coordination of Fe^{2+} with YH_2 was permitted to preferentially form a complex of Fe-YH_2. At this point, Fe^{2+} is in excess, and existing Fe^{2+} ions are not coordinated with EDTA-2Na. Stage II: $CuSO_4$ was added to the solution with pH = 2.83, leading to a coordination of Cu^{2+} with the COOH groups in the Fe-YH_2 complex to obtain Fe-YH_2-Cu, which was soluble in the solution. Considering that the ratio of –COOH groups to Cu^{2+} is approximately 2:1 (Table S1†), it is likely that one Cu atom may coordinate with two –COOH groups. Stage III: the addition of EDA resulted in a variation of pH from 2.83 to 10.83 in the solution.

Part I in stage III: in the process, the formation of COO^- groups derived from the COOH-Cu structure in the Fe-YH_2-Cu complex was retarded because the disassociation of Cu^{2+} from COOH-Cu should initially occur before the deprotonation process of COOH. As a result, part of Fe-YH_2 preferentially coordinated with the OH^- group instead of with the COO^- group (Fig. 1b), generating insoluble complexes including Y-Fe(OH)$_2$, which quickly precipitated. *Part II in stage III*: on account of the large molar ratio of EDA and EDTA (60:1) and the large coordination constants of EDA with Cu^{2+} ($\log K_{Y–Cu} < \log K_{EDA–Cu}$), the soluble complex of 2EDA–Cu formed and was dissociated from Fe-YH_2-Cu. The 2EDA–Cu complex was stable under conditions with a pH of 10,[27] and the residual amount of Fe^{2+} formed insoluble Fe(OH)$_2$ and EDA-Fe(OH)$_2$. In addition, soluble complexes containing Y–Fe, 2EDA–Fe, and 2EDA–Cu were simultaneously generated and then removed by centrifugation.

The obtained precipitates were washed and analyzed by infrared (IR) spectroscopy, which exhibited the characteristic peaks of Y and EDA, indicating the successful coordination of Fe^{2+} with Y and EDA (Fig. S1†). In addition, the detailed coordination behavior was explored by *in situ* XAS experiments. The peak centered around 1.7 Å was assigned to Fe–O(N) coordination due to the difficult distinction between Fe–O and Fe–N coordination in XAFS. During the preparation process before adding EDA, the XANES curves and Fourier transform curves showed that Fe and Cu were in the state of Fe^{2+} and
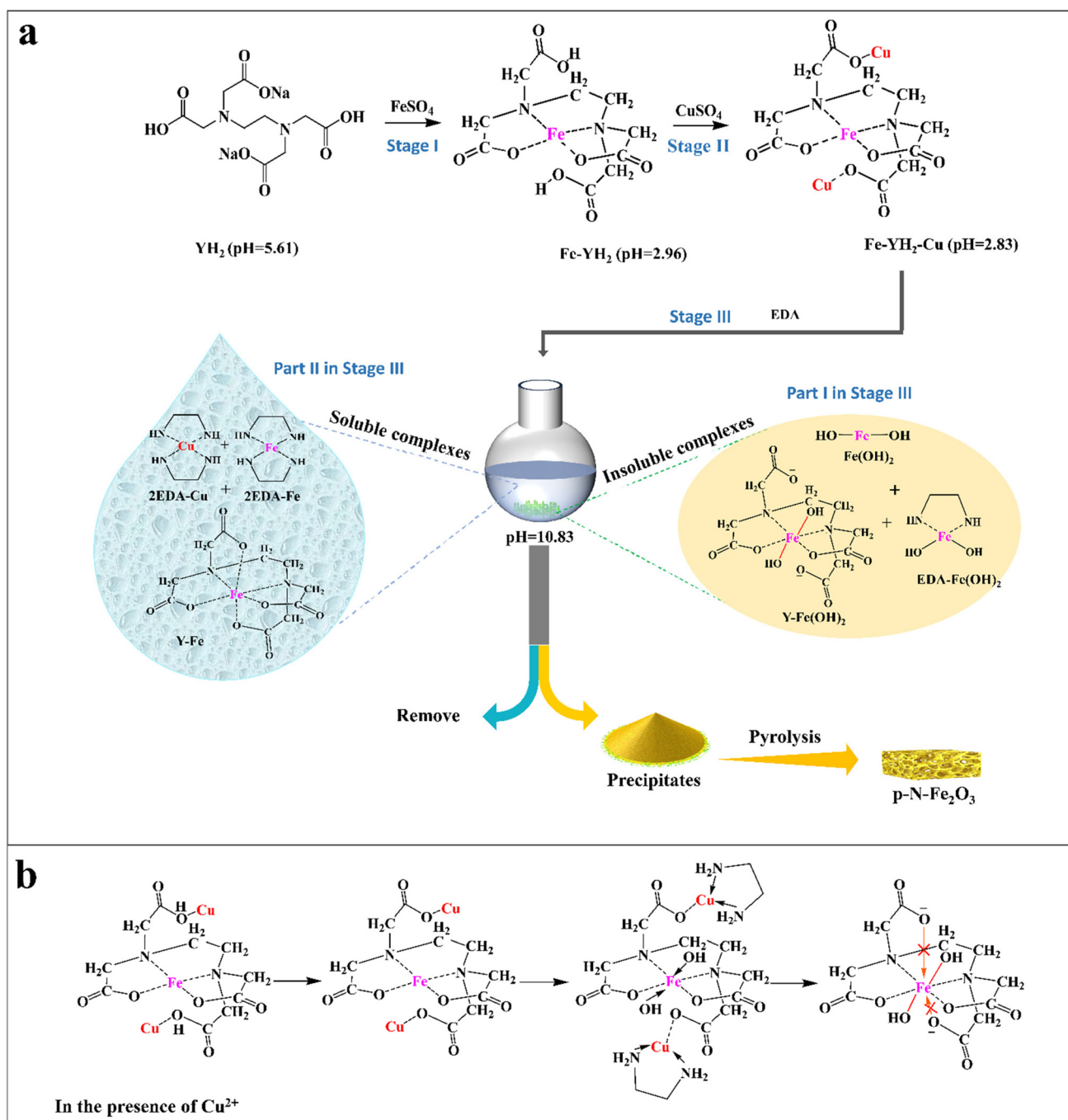
Fig. 1 Preparation of catalysts. (a) Details and mechanism for the preparation of catalyst p-N-Fe$_2$O$_3$. (b) Schematic diagram of the competitive coordination process in the preparation of p-N-Fe$_2$O$_3$ before pyrolysis. Notes: coordination constants in different stages: stage I, Fe(II)-YH$_2$: 1.568 ≈ Cu(II)-YH$_2$: 1.553, Cu(II)-COOH: 2.3; Fe(II)-COOH: non; stage II: Fe(II)−Y: 14.27 > Fe(II)-OH$_2$: 9.77 > Fe(II)−EDA: 7.65, Fe(II)-OH$_2$: 9.77 > Fe(II)-YH$_2$: 2.7, Cu(II)−EDA: 20 > Cu(II)−Y: 18.7 > Cu(II)-OH$_2$: 13.68.

Cu^{2+}, respectively (Fig. S2 and S3†).[28,29] Excess EDA preferentially coordinates with Cu^{2+} and Fe^{2+}, maintaining their oxidation states. Quantitative extended X-ray absorption fine structure (EXAFS) fitting analysis (Table S2†) revealed that there was a subtle variation in the coordination numbers of Fe–O/N after the addition of CuSO$_4$, demonstrating the stability of the Fe-YH$_2$ structure. The as-prepared precipitates were

pyrolyzed under N$_2$ to obtain a catalyst, which was denoted as p-N-Fe$_2$O$_3$.

To study the effect of the amount of Fe on the ratio of different components in the precipitates, we chose 75 mg, 100 mg, 150 mg, and 300 mg of FeSO$_4$ to investigate the composition under the same conditions. No precipitates were obtained under the condition of adding 75 mg FeSO$_4$ with an

equimolar amount of YH_2. The precipitation occurred when 100 mg, 150 mg, and 300 mg of $FeSO_4$ were used, and the precipitation precursors obtained were abbreviated as Fe-100, Fe-150, and Fe-300, respectively, and characterized using organic elemental analysis (OEA). The molar fraction of different components in different catalysts was calculated according to the OEA results, as shown in Fig. S4.†

The results demonstrated that the molar fraction of Y-Fe $(OH)_2$ increased with the amount of Fe, while the molar fractions of EDA-Fe$(OH)_2$ and Fe$(OH)_2$ slightly decreased. The excess amount of $FeSO_4$ resulted in an increasing molar fraction of Y-Fe$(OH)_2$ by inhibiting the formation of Cu-YH_2 and increasing the stability of Fe-YH_2-Cu. In addition, EDA was used to provide an alkaline environment for this method, and an excess amount of EDA was utilized to inhibit the formation of Cu$(OH)_2$ due to the larger coordination constant of EDA and Cu(II).

In addition, a control sample named $N-Fe_2O_3$ was also prepared under conditions free from $CuSO_4$ addition to investigate the competitive effects during coordination (Fig. S5†).

Under the circumstances, the saturated coordination of Fe^{2+} with YH_2 was permitted to form the complex of Fe-YH_2 in the presence of YH_2 and $FeSO_4$. However, the addition of EDA contributed to the change in solution to alkaline, which resulted in feasible coordination of the COO^- group with Fe^{2+} instead of coordination of the OH^- group with Fe^{2+} (Fe(II)–Y: 14.27 > Fe(II)-OH_2: 9.77). As a result, soluble complexes of Y–Fe and 2EDA–Fe were generated, and precipitates consisting of EDA-Fe(OH_2) and Fe$(OH)_2$ were obtained without Y-Fe$(OH)_2$. After separation and pyrolysis, the $N-Fe_2O_3$ catalyst was prepared. The obtained sediments showed no signal of symmetrical stretching vibration of C–O (1390 cm^{-1}) in the IR spectra, indicating the absence of a Y structure in $N-Fe_2O_3$, which was attributed to the nonexistence of the Y-Fe$(OH)_2$ complex in the precipitates before pyrolysis (Fig. S1†).

The as-prepared precipitates were pyrolyzed under an N_2 atmosphere to generate catalysts that were characterized by X-ray diffraction (XRD), as shown in Fig. 2a. The XRD patterns of all the catalysts were consistent with the characteristic peaks of pristine $\gamma-Fe_2O_3$ (PDF #39-1346), indicating that the
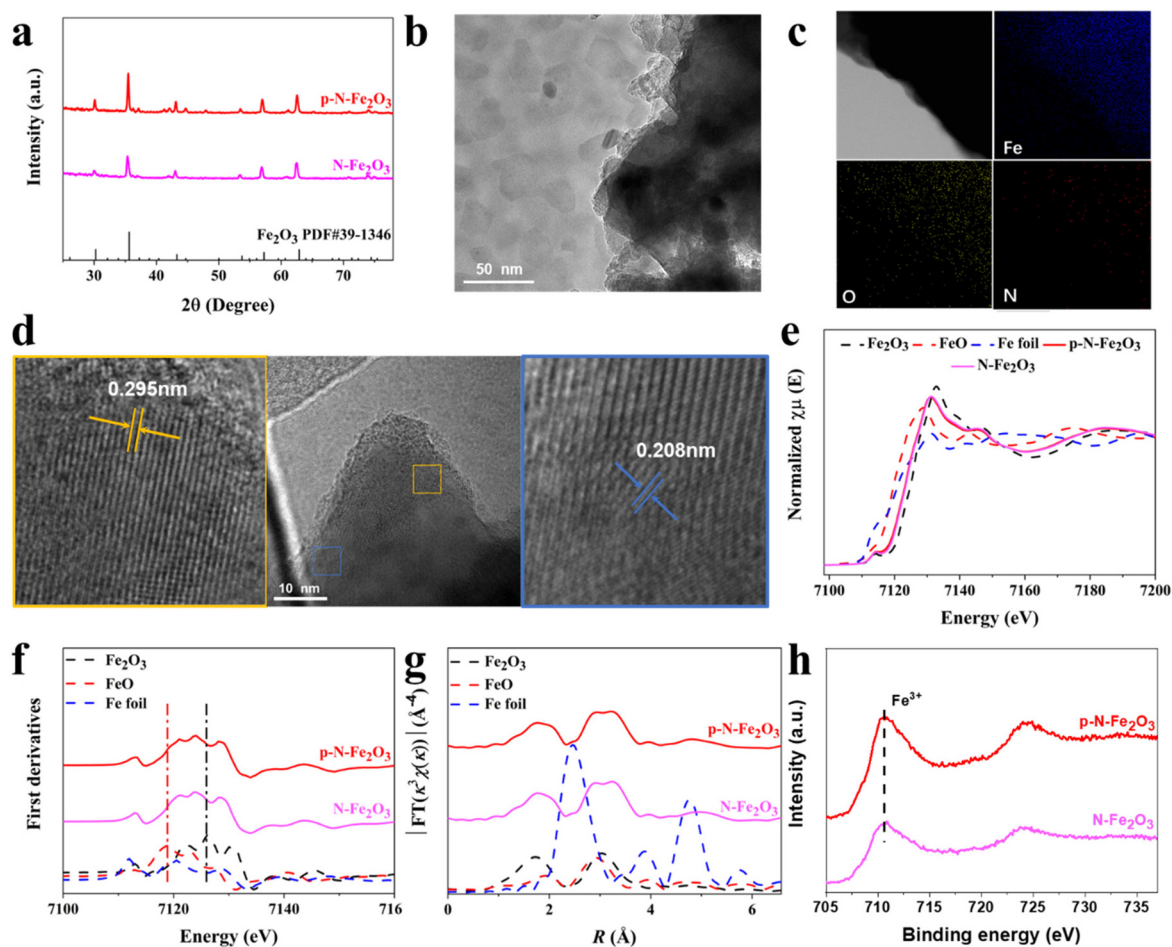

Fig. 2 Characterizations of the catalysts. (a) XRD patterns of $p-N-Fe_2O_3$ and $N-Fe_2O_3$. (b) TEM image of $p-N-Fe_2O_3$. (c) STEM image of $p-N-Fe_2O_3$ and the corresponding STEM-EDS elemental mapping images of Fe, O, and N of the region. (d) HRTEM images of $p-N-Fe_2O_3$. (e) Fe K-edge XANES spectra of $p-N-Fe_2O_3$, $N-Fe_2O_3$, Fe_2O_3, FeO, and Fe foil. (f) The first derivatives for $p-N-Fe_2O_3$, $N-Fe_2O_3$, Fe_2O_3, FeO, and Fe foil. (g) Fourier-transformed EXAFS spectra in R-space of $p-N-Fe_2O_3$, $N-Fe_2O_3$, Fe_2O_3, FeO, and Fe foil. (h) XPS spectra of $p-N-Fe_2O_3$ and $N-Fe_2O_3$ in Fe 2p.

main component of the obtained catalysts was γ-Fe_2O_3, and slight differences were observed between those of p-N-Fe_2O_3 and N-Fe_2O_3. Transmission electron microscopy (TEM) and scanning electron microscopy (SEM) were used to study the morphologies of the catalysts. The morphologies of p-N-Fe_2O_3 and N-Fe_2O_3 exhibited a bulk structure composed of nanoparticles with a size distribution of 50–100 nm, as shown in Fig. 2b, and Fig. S6, S7,† respectively.

Scanning transmission electron microscopy-energy dispersive X-ray spectroscopy (STEM-EDS) demonstrated the existence of elemental Fe, N, and O in p-N-Fe_2O_3 and N-Fe_2O_3 (Fig. 2c and Fig. S8†). The element Fe was the main component in the catalyst, and the results were similar to those detected by inductively coupled plasma optical emission spectrometry (ICP-OES) (Table S3†), and the element Cu was not detected by ICP-OES. In the high-resolution TEM (HRTEM) of p-N-Fe_2O_3 (Fig. 2d), the emerged fringe spacings of 0.208 nm and 0.295 nm were well matched with the (400) and (220) lattice planes of γ-Fe_2O_3, and the results were in accordance with those of XRD.

The detailed coordination environment of Fe atoms in the catalysts was explored using X-ray absorption spectroscopy (XAS).[30,31] The K-edge X-ray absorption near edge structure (XANES) curves and the derivatives of the catalysts (Fig. 2e and f) showed that the element Fe was in the state between Fe^{2+} and Fe^{3+}. The edge of the XANES spectra of the N-doped Fe_2O_3 samples (p-N-Fe_2O_3 and N-Fe_2O_3) shifted towards a lower energy as compared to that of pristine Fe_2O_3, suggesting a negative charge state of Fe atoms in the as-prepared catalysts.

The Fourier transform (FT) curves at the Fe K-edge of the extended X-ray adsorption fine structure (EXAFS) spectra were further fitted to study the coordination information for Fe atoms, as shown in Fig. 2g. The peak at 2–3 Å was well matched with the Fe–Fe bond in Fe_2O_3.[32,33] The doping of N in Fe_2O_3 resulted in the wide peaks of Fe–O/N and Fe–Fe in p-N-Fe_2O_3, which shifted towards a higher energy as compared to that of Fe_2O_3, indicating the variation in the electronic states of the element Fe in the catalysts.[34,35] It is worth noting that signals of elemental Cu and corresponding peaks were not observed. Furthermore, the XAS data were fitted to explore the detailed coordination information of the element Fe in different catalysts (Table S4†). It was discovered that the coordination number of Fe–O/N in p-N-Fe_2O_3 and N-Fe_2O_3 was lower compared to pristine Fe_2O_3, suggesting the presence of oxygen vacancies and defects in both of the obtained catalysts.

The electronic states of Fe in the catalysts were also analysed by XPS. The XPS spectra of p-N-Fe_2O_3 showed the existence of the elements Fe, O, N, and C in the catalyst (Fig. S9a†), and there was no characteristic peak of Cu in the spectra (Fig. S9b†), which was in accordance with the results characterized by XAS and ICP methods. As illustrated in Fig. 2h, the peaks at 710.8 eV and 724.8 eV in the Fe 2p spectra indicated that Fe atoms in the catalyst existed in the state of Fe^{3+}.[36,37] The high-resolution O 1s spectra of p-N-Fe_2O_3 and N-Fe_2O_3 were assigned to three components corresponding to lattice oxygen (approximately 530 eV), oxygen vacancy (531.5 eV), and

surface-adsorbed oxygen species (533.5 eV) (Fig. S9c†).[38,39] The N dopant resulted in facile generation of surface defects, such as oxygen vacancy, which was observed in the high-resolution O 1s spectra of these two catalysts. As displayed in Fig. S9d,† the elemental N in the catalysts mainly existed in the form of pyridinic N (398.1 eV) and Fe–N coordination with pyridine (399.6 eV).[40]

^{57}Fe Mössbauer spectroscopy is sensitive to the electronic states of Fe with a similar coordination environment, which is an efficient method for the study of the valence state and the magnetic structure of Fe in catalysts.[41] The p-N-Fe_2O_3 and N-Fe_2O_3 catalysts were further characterized by ^{57}Fe Mössbauer spectroscopy, and the results are illustrated in Fig. 3. The spectra of p-N-Fe_2O_3 was fitted into two types of sextets that were attributed to the γ-Fe_2O_3 phase and N-doped Fe_2O_3. According to the values of isomer shift (IS) and quadrupole splitting (QS) (Table S5†), N-doped Fe_2O_3 was denoted as $FeO_{1.5-x}N_x$ ($0.34 < x < 0.54$) sites in p-N-Fe_2O_3.

The hyperfine field (H) in the components of the $FeO_{1.5-x}N_x$ ($H = 46.08$) phase was slightly different from that of γ-Fe_2O_3 ($H = 49.63$), which was attributed to the incorporation of a small amount of N in the γ-Fe_2O_3. Similar sextets attributed to $FeO_{1.5-y}N_y$ ($0.34 < y < 0.54$) sites in N-Fe_2O_3 were also detected. However, a doublet attributed to the FeN_4 phase was observed in the Mössbauer transmission spectra of N-Fe_2O_3.[42] The absence of the doublet component in the Mössbauer spectrum of p-N-Fe_2O_3 demonstrated the absence of the FeN_4 phase. In addition, it is noteworthy that obvious differences in quadrupole splitting (QS) were found for N–Fe–O sites in different catalysts, as shown in Table S5.†

The QS describes the axially symmetric deviation from the spherical shape of the positive charge distribution in the nucleus, which could exert an ulterior influence on the charge around the nucleus. A positive QS value (QS > 0) indicates that the charge distribution is elongated at the poles (prolate shape), exhibiting a cigar shape. In other words, if the charge distribution is compressed at the poles (oblate shape) showing a pancake shape, the value of the QS is negative (QS < 0).[43] The distortion of the Fe–O coordination derived from the doping of N into Fe_2O_3 may have an obvious influence on the QS.[44–47] Herein, the Fe ion spin states did not change according to the small QS value (QS < 1 mm s^{-1}). In p-N-Fe_2O_3, the QS value of $FeO_{1.5-x}N_x$ (QS = −0.02) was negative, which was different from
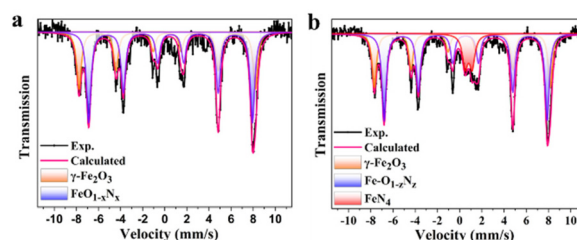

Fig. 3 ^{57}Fe Mössbauer spectroscopy of the catalysts. (a) p-N-Fe_2O_3. (b) N-Fe_2O_3.

that of $FeO_{1.5-y}N_y$ (QS = 0.01). It can be concluded that the differences were caused by various N-doping sites in Fe_2O_3. The different N-doping strategies resulted in various iron-coordination components and Fe–O–N sites. An H-type cell was used to evaluate the performance of the catalysts for the CO_2RR. Ionic liquid (IL)-based electrolyte (1-butyl-3-methylimidazolium hexafluorophosphate ([Bmim]PF$_6$/acetonitrile (MeCN)/H$_2$O (w/w/w = 30/65/5))) was used. It was previously reported that IL exhibited the ability to reduce the reaction barrier for CO_2 activation and suppress the hydrogen evolution reaction (HER).[48] The linear sweep voltammetry (LSV) curves of different catalysts in CO_2- or N_2-saturated electrolytes are illustrated in Fig. S10.† In the CO_2-saturated electrolyte, higher current densities were obtained at the potential ranging from −0.6 V to −2.8 V vs. Ag/Ag$^+$, indicating that the catalysts were highly active for CO_2RR. Therefore, the potential ranging from −1.9 V to −2.6 V vs. Ag/Ag$^+$ was selected as the reaction potential.

The gaseous and liquid products were collected and analyzed by gas chromatography (GC) and ^{1}H NMR, respectively. Only gas products were detected in the experiment. As shown in Fig. 4a, H$_2$, CH$_4$, C$_2$H$_4$, and C$_2$H$_6$ were produced over p-N-Fe$_2$O$_3$. At −2.0 V vs. Ag/Ag$^+$, the FE of C$_2$ products reached 60.8%, and the current density of C$_2$ products was 39.1 mA cm^{-2}, which is the highest result for non-copper catalysts in an H-cell (Fig. S11†).[8,12,49–52] The HER was the predominant side reaction in this process as the potential became more negative. Additionally, the FE of C2 products gradually decreased with enhanced H$_2$ production.

During the preparation of p-N-Fe$_2$O$_3$, a reduction in the iron content resulted in a significant enhancement of the HER
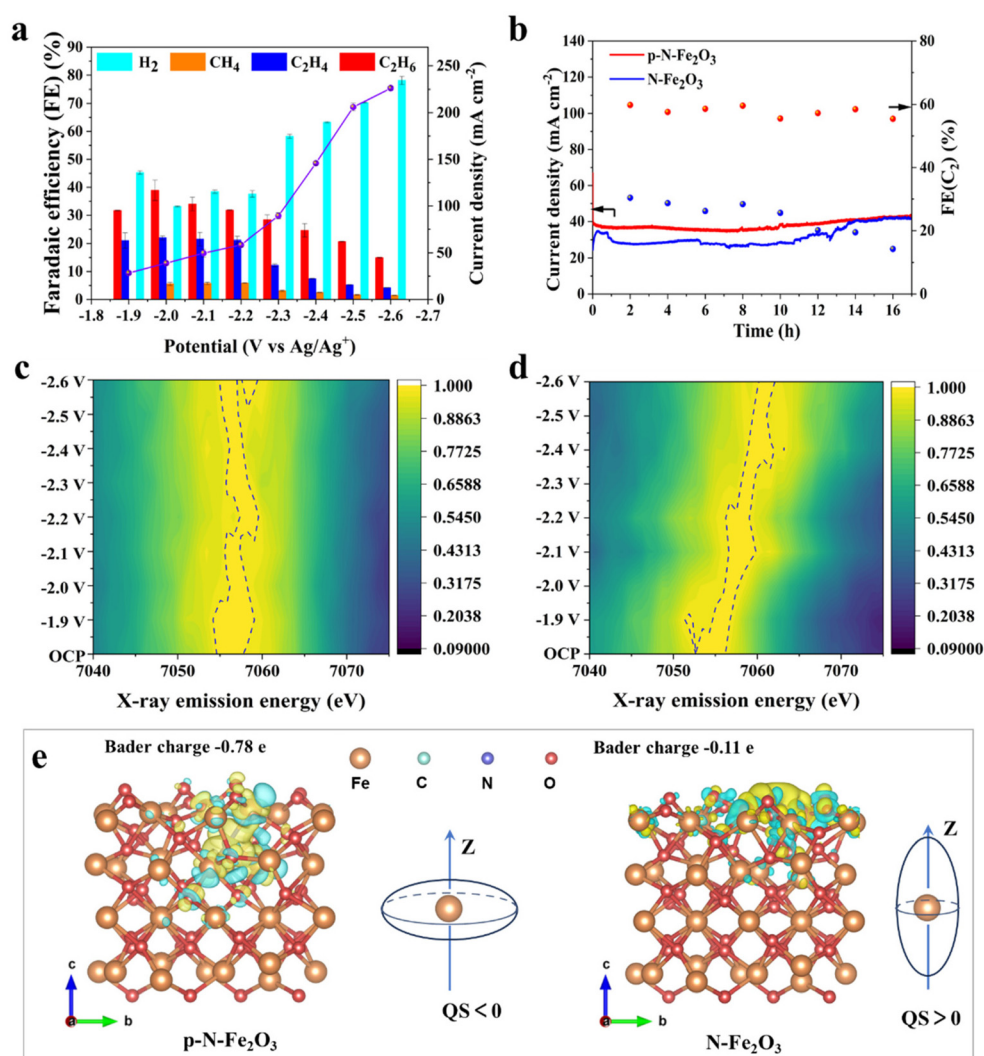

Fig. 4 Electrochemical properties study and the charge density difference of catalysts. (a) Catalytic performances of p-N-Fe$_2$O$_3$. (b) Long-term stability of CO_2 electroreduction over p-N-Fe$_2$O$_3$ and N-Fe$_2$O$_3$. (c) *In situ* X-ray emission spectroscopy for p-N-Fe$_2$O$_3$ at the potential ranging from −1.9 V to −2.6 V vs. Ag/Ag$^+$. (d) *In situ* X-ray emission spectroscopy for N-Fe$_2$O$_3$ at the potential ranging from −1.9 V to −2.6 V vs. Ag/Ag$^+$. (e) The corresponding differential charge densities and Bader charges for p-N-Fe$_2$O$_3$ and N-Fe$_2$O$_3$. The yellow and cyan surfaces correspond to the charge gain and lost regions, respectively.

and an obvious decrease in carbonaceous products (Fig. S12†). For comparison, we evaluated the performance of N-Fe_2O_3 under the same conditions. For the N-Fe_2O_3 catalyst, the FE of C_2 products was 20%, and the current density decreased to 10 mA cm^{-2}, with CO as the main product (Fig. S13†). A control experiment was conducted under the same conditions using N_2-saturated electrolyte, but no carbonaceous products were detected. The CO_2RR origin of the products was confirmed by measuring isotope-labelled $^{13}CO_2$ (Fig. S14†).

We also evaluated the catalytic performance of p-N-Fe_2O_3 in 0.1 M $KHCO_3$ (Fig. S15†) and observed the formation of multi-carbon products. However, because of the pronounced HER, the FE of C_2 products was relatively low. This further demonstrated that ionic liquid played a critical role in suppressing the HER. Thus, the p-N-Fe_2O_3 catalyst containing $FeO_{1.5-x}N_x$ sites boosted the production of C_2 products. Significantly, the p-N-Fe_2O_3 catalyst without FeN_4 sites exhibited no production of CO. However, the N-Fe_2O_3 catalyst containing partial FeN_4 sites exhibited a tendency to generate CO. Furthermore, the C_2 selectivity was obviously low.

The results verified the conclusion that the coexistence of FeN_4 in γ-Fe_2O_3 nanoparticles resulted in facile production of CO and was not favorable to C–C coupling. As reported, the CO selectivity over FeN_4 sites was attributed to the adsorption of CO_2 on the FeN_4 sites together with the acceleration of *COOH intermediate formation.[53,54] The long-term stability over p-N-Fe_2O_3 and N-Fe_2O_3 were estimated at −2.0 V $vs.$ Ag/Ag^+. The FE of C_2 products and the current density over p-N-Fe_2O_3 showed no obvious change after 16 h, indicating the excellent stability during the CO_2RR. However, when using N-Fe_2O_3 as the electrode, the FE clearly decreased after a period of time, as shown in Fig. 4b.

To explore the nature of the performance of various catalysts during the CO_2RR, in situ X-ray emission spectroscopy (XES) was also performed. As displayed in Fig. 4c, the signals of p-N-Fe_2O_3 inconspicuously changed at different potentials, indicating that elemental Fe maintained the Fe^{3+} state during the CO_2RR. However, the signals of Fe in N-Fe_2O_3 gradually shifted to high energy at more negative potentials, signifying that partial Fe^{3+} was continuously reduced (Fig. 4d). The various N occupancies resulted in different distortions of Fe–O coordination and the oxygen vacancy in the two catalysts, which influenced the stability of the catalysts.

To further investigate the stability of p-N-Fe_2O_3, we characterized the catalyst using XRD, TEM, SEM, and EDS mapping before and after the reaction (Fig. S16†). The results indicated that the difference in the structure and morphology of the catalyst before and after the reaction was not notable, which signified the excellent stability of p-N-Fe_2O_3 during the reaction process. Additionally, the coordination number of Fe–O in FeO and Fe_2O_3 is 6, indicating that the coordination number is due to oxygen vacancies and defects rather than a mixture of iron oxides not being Fe_2O_3.[55]

The electrochemically active surface area (ECSA) of the catalysts was estimated by fitting the double electric layer capacitance of the different catalysts (Fig. S17†). The higher double-layer capacitance value of p-N-Fe_2O_3 (53.57 mF cm^{-2}) compared with N-Fe_2O_3 (42.9 mF cm^{-2}) indicates that there is a higher electrochemical surface area for p-N-Fe_2O_3.[56] The Nyquist plots under open circuit potential in CO_2-saturated electrolyte were used to determine the properties of the electrode/electrolyte interface (Fig. S18†). The values for the interfacial charge transfer resistance (R_{ct}) were obtained by fitting the experimental impedance data using Randles equivalent circuit $R (C(R(Q(RW))))$, as illustrated in Fig. S19.†[57] The interfacial charge transfer resistance was lower for the p-N-Fe_2O_3 catalyst as compared with N-Fe_2O_3, indicating the facile charge transfer over p-N-Fe_2O_3, which was attributed to the appropriate N occupancies in Fe_2O_3.

The results were also in accordance with the electronic states of Fe characterized by ^{57}Fe Mössbauer spectroscopy. Various N–Fe–O components were formed due to the different N neighbours of Fe atoms in the lattice, which resulted in a different iron electron structure, leading to the different activities and selectivities of the CO_2RR. $FeO_{1-x}N_x$ sites in p-N-Fe_2O_3 displayed a negative QS value, resulting in a compressed charge distribution around the poles of the Fe nucleus, which facilitated the charge transfer. However, the N-Fe_2O_3 catalyst containing N–Fe–O sites with other N occupancies in Fe_2O_3 displayed an elongated charge distribution around the poles of the Fe nucleus. Therefore, the electronic states of Fe exhibited a low ability for charge transfer. In addition, the coexistence of FeN_4 sites facilitated the desorption of *CO,[58] resulting in C_2 production with low efficiency.

On the basis of the above analysis, DFT studies were carried out to identify and characterize the atomic sites in iron-based catalysts for promoting the selectivity of C_2 products. According to the properties of the N–Fe–O sites obtained by various experiments, two catalyst models were constructed based on the QS values derived from the ^{57}Fe Mössbauer spectroscopy, as shown in Fig. S20.† The desorption free energy of the *CO intermediate over p-N-Fe_2O_3 is higher than that over N-Fe_2O_3, as illustrated in Fig. S21.† The difficult desorption of *CO leads to low selectivity for CO, which is consistent with the experimental results. Additionally, the corresponding charge density difference of the various catalysts is shown in Fig. 4e, which indicates that different N occupancies in Fe_2O_3 result in an alteration of charge distribution around the Fe atom. The delocalized electron transfer from the Fe atoms to the N–Fe–O interface was also confirmed by Bader charge analysis (Fig. 4e). Images from other views are provided in Fig. S22.†

An electron-rich interface for p-N-Fe_2O_3 is formed because of the delocalized electron transfer from Fe atoms at N–Fe–O sites, which greatly facilitates the adsorption and activation of the *CO intermediate promoting C–C coupling. Thus, the electronic effects of the N–Fe–O sites resulted in increased selectivity toward C_2 products compared with the N-Fe_2O_3 catalyst. Additionally, the Fe-d states of the catalysts distinctly changed as a result (Fig. S23†). Thus, the $FeO_{1-x}N_x$ sites in the p-N-Fe_2O_3 catalyst, which have compressed charge distribution around the poles of the Fe nucleus, facilitate the adsorption of *CO intermediate and C–C coupling in the CO_2RR.

To further exclude the effect of copper on the production of C_2 products, we prepared corresponding catalysts using Ni and Cd salts as substitutes for Cu salt, and conducted characterization and performance tests (Fig. S24 and S25†). The characterization indicated that there were no remaining Ni/Cd elements in the catalysts. The faradaic efficiency of C_2 products over the two catalysts prepared with elemental Ni and Cd was 55.31% and 59.7%, respectively, which were comparable to those of p-N-Fe_2O_3. This further confirmed that the production of C_2 products was not attributed to Cu.

Conclusions

The p-N-Fe_2O_3 catalyst containing $FeO_{1−x}N_x$ sites and free of FeN_4 sites is very efficient for producing C_2 product in the CO_2RR. The FE of C_2 products can reach 60.8% with a current density of 39.1 mA cm^{-2}, which is currently the best result for non-copper catalysts in an H-cell. In contrast, the N-Fe_2O_3 catalyst possessing FeN_4 and $FeO_{1−y}N_y$ sites with different N occupancies in Fe_2O_3 showed an FE_{C_2} of 20% with a current density of 10 mA cm^{-2} under the same reaction conditions, which is much lower than that of the catalysts without FeN_4 sites. The high selectivity of C_2 products was attributed to the electron-rich interface of the p-N-Fe_2O_3 catalyst that is formed by delocalizing electron transfer from Fe atoms in N–Fe–O sites. Thus, the adsorption and activation of the *CO intermediate are greatly facilitated. As a result, the process of C–C coupling is promoted. The relationship of N occupancies and selectivity towards C_2 products over the iron-based catalyst is very helpful for exploration of new non-Cu electrocatalysts for the CO_2RR to produce C_2 products.

Author contributions

Peng Chen and Pei Zhang: catalyst synthesis and characterisations. Xinchen Kang, Jun Ma, Chunjun Chen, and Xing Tong: electro-reduction of CO_2. Xueqing Xing, Zhonghua Wu, and Lirong Zheng: collection of in situ XES and XAS data. Zhimin Liu and Shiqiang Liu: DFT calculations. Pei Zhang and Buxing Han: overall design and direction of the project. Peng Chen, Pei Zhang, and Buxing Han: preparation of the manuscript with assistance from all authors.

Data availability

All data generated or analyzed in this study are included in this manuscript and the ESI.† The datasets used and/or analyzed in this study are available upon request from the corresponding authors.

Conflicts of interest

There are no conflicts to declare.

Acknowledgements

References

1 M. T. McCulloch, A. Winter, C. E. Sherman and J. A. Trotter, Nat. Clim. Change, 2024, 14, 171–177.

2 R. C. DiDomenico, K. Levine, C. Bundschu, L. Reimanis, T. Arias and T. Hanrath, ACS Catal., 2024, 14, 785–796.

3 W. C. Ma, S. J. Xie, T. T. Liu, Q. Y. Fan, J. Y. Ye, F. F. Sun, Z. Jiang, Q. H. Zhang, J. Cheng and Y. Wang, Nat. Catal., 2020, 3, 478–487.

4 S. Yang, H. Y. An, S. Arnouts, H. Wang, X. Yu, J. de Ruiter, S. Bals, T. Altantzis, B. M. Weckhuysen and W. van der Stam, Nat. Catal., 2023, 6, 796–806.

5 Z. F. Li, L. Q. Wang, L. C. Sun and W. X. Yang, J. Am. Chem. Soc., 2024, 146, 23901–23908.

6 C. Kim, T. Eom, M. S. Jee, H. Jung, H. Kim, B. K. Min and Y. J. Hwang, ACS Catal., 2017, 7, 779–785.

7 J. Timoshenko, A. Bergmann, C. Rettenmaier, A. Herzog, R. M. Arán Ais, H. S. Jeon, F. T. Haase, U. Hejral, P. Grosse, S. Kühl, E. M. Davis, J. Tian, O. Magnussen and B. R. Cuenya, Nat. Catal., 2022, 5, 259–267.

8 L. Ji, L. Li, X. Q. Ji, Y. Zhang, S. Y. Mou, T. W. Wu, Q. Liu, B. H. Li, X. J. Zhu, Y. L. Luo, X. F. Shi, A. M. Asiri and X. P. Sun, Angew. Chem., Int. Ed., 2020, 59, 758–762.

9 S. Cao, S. Wei, X. Wei, S. Zhou, H. Chen, Y. Hu, Z. Wang, S. Liu, W. Guo and X. Lu, Small, 2021, 17, 2100949.

10 F. Li, H. Wen and Q. Tang, J. Mater. Chem. A, 2022, 10, 13266–13277.

11 K. Guo, H. Lei, X. Li, Z. Zhang, Y. Wang, H. Guo, W. Zhang and R. Cao, Chin. J. Catal., 2021, 42, 1439–1444.

12 L. Ji, L. Chang, Y. Zhang, S. Y. Mou, T. Wang, Y. L. Luo, Z. M. Wang and X. P. Sun, ACS Catal., 2019, 9, 9721–9725.

13 L. Wang, X. Lai, Y. Xu, S. Luo, L. Wang, K. Yan, D. Zhang, S. Feng and Y. Xu, Catal. Sci. Technol., 2023, 13, 3946–3952.

14 M. Ma and Q. Tang, J. Mater. Chem. C, 2022, 10, 15948–15956.

15 F. Pan, H. Zhang, K. Liu, D. Cullen, K. More, M. Wang, Z. Feng, G. Wang, G. Wu and Y. Li, ACS Catal., 2018, 8, 3116–3122.

16 L. Lin, H. Li, C. Yan, H. Li, R. Si, M. Li, J. Xiao, G. Wang and X. Bao, Adv. Mater., 2019, 31, 1903470.

17 J. Tuo, Y. Zhu, H. Jiang, J. Shen and C. Li, ChemElectroChem, 2020, 7, 4767–4772.

18 S. Cao, S. Zhou, H. Chen, S. Wei, S. Liu, X. Lin, X. Chen, Z. Wang, W. Guo and X. Lu, Energy Environ. Mater., 2023, 6, e12287.

19 P. Chen, P. Zhang, X. Kang, L. Zheng, G. Mo, R. Wu, J. Tai and B. Han, *J. Am. Chem. Soc.*, 2022, **144**, 14769–14777.

20 Y. S. Zhou, F. L. Che, M. Liu, C. Q. Zou, Z. Q. Liang, P. De Luna, H. F. Yuan, J. Li, Z. Q. Wang, H. P. Xie, H. M. Li, P. N. Chen, E. Bladt, R. Q. Bermudez, T. K. Sham, S. Bals, J. Hofkens, D. Sinton, G. Chen and E. H. Sargent, *Nat. Chem.*, 2018, **10**, 974–980.

21 R. Kas, R. Kortlever, H. Yilmaz, M. T. M. Koper and G. Mul, *ChemElectroChem*, 2015, **2**, 354–358.

22 X. G. Zhang, S. Feng, C. Zhan, D. Y. Wu, Y. Zhao and Z. Q. Tian, *J. Phys. Chem. Lett.*, 2020, **11**, 6593–6599.

23 M. Zheng, P. Wang, X. Zhi, K. Yang, Y. Jiao, J. Duan, Y. Zheng and S. Z. Qiao, *J. Am. Chem. Soc.*, 2022, **144**, 14936–14944.

24 A. E. Martell and R. M. Smith, *Critical stability constants, Vol. I, Amino acids*, Springer, 1974, pp. 204–209.

25 X. Hua, J. Hu, X. Jiang, D. Dong, Z. Guo and D. Liang, *Environ. Sci. Pollut. Res.*, 2013, **20**, 1079–1088.

26 H. Zhao, Z. Zhang, F. Shemshaki, J. Zhang and Z. Ring, *Energy Fuels*, 2006, **20**, 1822–1827.

27 A. Keivanloo, M. Bakherad, M. Khosrojerdi and A. H. Amin, *Res. Chem. Intermed.*, 2018, **44**, 2571–2583.

28 P. Wang, T. Li, Q. Wu, R. Du, Q. Zhang, W. H. Huang, C. L. Chen, Y. Fan, H. Chen and Y. Jia, *ACS Nano*, 2022, **16**, 17021–17032.

29 Y. P. Huang, C. W. Tung, T. L. Chen, C. S. Hsu, M. Y. Liao, H. C. Chen and H. M. Chen, *Nanoscale*, 2022, **14**, 8944–8950.

30 V. A. Saveleva, K. Kumar, P. Theis, N. S. Salas, U. I. Kramm, F. Jaouen, F. Maillard and P. Glatzel, *ACS Appl. Energy Mater.*, 2023, **6**, 611–616.

31 T. A. Hamdalla, A. M. Aboraia, V. Shapovalov, A. Guda, N. Kosova, O. Podgornova, A. Darwish, S. Al Ghamdi, S. Alfadhli and A. M. Alatawi, *Sci. Rep.*, 2023, **13**, 2169.

32 A. Boubnov, A. Roppertz, M. D. Kundrat, S. Mangold, B. Reznik, C. R. Jacob, S. Kureti and J. D. Grunwaldt, *Appl. Surf. Sci.*, 2016, **386**, 234–246.

33 Z. Yang, Y. Wang, M. Zhu, Z. Li, W. Chen, W. Wei, T. Yuan, Y. Qu, Q. Xu and C. Zhao, *ACS Catal.*, 2019, **9**, 2158–2163.

34 Y. Qiao, P. Yuan, Y. Hu, J. Zhang, S. Mu, J. Zhou, H. Li, H. Xia, J. He and Q. Xu, *Adv. Mater.*, 2018, **30**, 1804504.

35 A. Sundman, T. Karlsson, H. Laudon and P. Persson, *Chem. Geol.*, 2014, **364**, 93–102.

36 D. Zhou, L. Yang, L. Yu, J. Kong, X. Yao, W. Liu, Z. Xu and X. Lu, *Nanoscale*, 2015, **7**, 1501–1509.

37 V. Maheskumar, K. Saravanakumar, Y. Yea, Y. Yoon and C. M. Park, *Int. J. Hydrogen Energy*, 2023, **48**, 5080–5094.

38 S. Deng, R. Chen, G. Li, Z. Xia, M. Zhang, W. Zhou, M. Wong and H. S. Kwok, *IEEE Trans. Electron Devices*, 2017, **64**, 3174–3182.

39 E. S. Calipari, A. Godino, E. G. Peck, M. Salery, N. L. Mervosh, J. A. Landry, S. J. Russo, Y. L. Hurd, E. J. Nestler and D. D. Kiraly, *Nat. Commun.*, 2018, **9**, 9.

40 H. Zhang, J. Li, S. Xi, Y. Du, X. Hai, J. Wang, H. Xu, G. Wu, J. Zhang and J. Lu, *Angew. Chem.*, 2019, **131**, 15013–15018.

41 J. Li, M. T. Sougrati, A. Zitolo, J. M. Ablett, I. C. Oğuz, T. Mineva, I. Matanovic, P. Atanassov, Y. Huang and I. Zenyuk, *Nat. Catal.*, 2021, **4**, 10–19.

42 U. I. Koslowski, I. A. Wurmbach, S. Fiechter and P. Bogdanoff, *J. Phys. Chem. C*, 2008, **112**, 15356–15366.

43 G. R. Hoy, in *Encyclopedia of physical science and technology*, ed. R. A. Meyers, Academic Press, 3rd edn, 2003, pp. 173–187.

44 E. Yuryeva and M. Oshtrakh, *Hyperfine Interact.*, 2008, **181**, 37–43.

45 L. P. Li, Q. Wei, X. L. Ren, W. C. Li and W. H. Su, *Phys. Status Solidi B*, 1995, **187**, 225–230.

46 L. P. Li, G. S. Li, X. Y. Song, J. P. Miao, X. F. Zhou and W. H. Su, *Chin. Phys. Lett.*, 1998, **15**, 925.

47 D. Borsa and D. Boerma, *Hyperfine Interact.*, 2003, **151**, 31–48.

48 J. Yang, J. Jiao, S. Liu, Y. Yin, Y. Cheng, Y. Wang, M. Zhou, W. Zhao, X. Tong and L. Jing, *Angew. Chem., Int. Ed.*, 2024, **63**, e202410145.

49 Y. Song, W. Chen, C. Zhao, S. Li, W. Wei and Y. Sun, *Angew. Chem., Int. Ed.*, 2017, **56**, 10840–10844.

50 Y. Liu, S. Chen, X. Quan and H. Yu, *J. Am. Chem. Soc.*, 2015, **137**, 11631–11636.

51 J. Ding, H. B Yang, X. L. Ma, S. Liu, W. Liu, Q. Mao, Y. Huang, J. Li, T. Zhang and B. Liu, *Nat. Energy*, 2023, **8**, 1386–1394.

52 J. Yin, Z. Yin, J. Jin, M. Sun, B. Huang, H. Lin, Z. Ma, M. Muzzio, M. Shen and C. Yu, *J. Am. Chem. Soc.*, 2021, **143**, 15335–15343.

53 J. Gu, C. S. Hsu, L. Bai, H. M. Chen and X. Hu, *Science*, 2019, **364**, 1091–1094.

54 J. Lei and T. Zhu, *ACS Catal.*, 2024, **14**, 3933–3942.

55 O. Bakieva and O. Nemtsova, *J. Electron Spectrosc. Relat. Phenom.*, 2018, **222**, 15–23.

56 X. Kang, B. Wang, K. Hu, K. Lyu, X. Han, B. F. Spencer, M. D. Frogley, F. Tuna, E. J. McInnes and R. A. Dryfe, *J. Am. Chem. Soc.*, 2020, **142**, 17384–17392.

57 Q. Zhu, D. Yang, H. Liu, X. Sun, C. Chen, J. Bi, J. Liu, H. Wu and B. Han, *Angew. Chem.*, 2020, **132**, 8981–8986.

58 X. Li, S. Xi, L. Sun, S. Dou, Z. Huang, T. Su and X. Wang, *Adv. Sci.*, 2020, **7**, 2001545.